Experimental and DFT insights of Zn-doping effects on the visible-light photocatalytic water splitting and dye decomposition over Zn-doped BiOBr photocatalysts

Junqiu Guo[a], Xin Liao[a], Ming-Hsien Lee[b], Geoff Hyett[c], Chung-Che Huang[d], Daniel W. Hewak[d], Sakellaris Mailis[d], Wei Zhou[a, e], Zheng Jiang [a]*

[a.] Faculty of Engineering and the Environment, University of Southampton, Southampton, SO17 1BJ, UK

[b.] Department of Physics, Tamkang University, Taipei 25137, Taiwan, R.O. China

[c.] Department of Chemistry, University of Southampton, Southampton, SO17 1BJ, UK

[d.] Optoelectronics Research Centre, University of Southampton, Southampton, SO17 1BJ, UK

[e.] Key Laboratory of Functional Inorganic Material Chemistry, Ministry of Education of PR China, Heilongjiang University, Harbin, 150080, PR China

Abstract

Synergetic experimental and DFT insights of energy band structures and photogenerated reactive intermediates are indispensable to design impurity-doped photocatalysts for photocatalytic environment remediation and solar fuels. Herein, despite the larger bandgap (Eg), Zn-doped BiOBr samples exhibited superior activity to BiOBr in the photocatalytic water splitting but adverse in photodegradation of Rhodamine B under visible-light illumination. Based on the spectral and electrochemical impedance characterisations and DFT simulations, the broader bandgap of Zn-doped BiOBr was explicitly assigned to more positive valence band maximum (VBM) and more negative conduction band minimum (CBM). The enhanced photocatalytic water splitting on Zn-doped BiOBr was assigned to the higher redox chemical potentials of charge carriers on respective CBM and VBM, suppressed back reaction and reduced recombination of photogenerated charge carriers. However, the reduced e^--h^+ recombination on Zn-doped BiOBr cannot cancel the adverse influences of its weaker light absorption and dye-sensitisation effects, leading to slower RhB photodegradation.

Keywords: photocatalysis, Zn-doped BiOBr, photoelectrochemistry, band structure, DFT

1. Introduction

The ever-increasing concerns of energy and environment sustainability have motivated great enthusiasm in photocatalytic environment remediation and artificial photosynthesis that require rational design of effective visible-light photocatalysts and understanding of their working mechanism. The bismuth oxybromide (BiOBr) compound semiconductor has emerged recently as a stable and active visible-light photocatalyst with an indirect bandgap of 2.6~2.9 eV [1-3]. The BiOBr is of a tetragonal crystal structure, constructed by alternative stacks of $[Bi_2O_2]^{2+}$ slabs and double Br^- slabs through Van de Waals interaction. Between the constituent $[Bi_2O_2]^{2+}$ and $2[Br^-]$ slabs, there exist

intrinsic built-in static electric fields that were thought able to promote separation of photogenerated electrons (e^{-1}) and holes (h^{+}) across CBM and VBM [4-6] and beneficial to their transportation to catalyst surface for participating redox reactions or depression of recombination otherwise [7-9]. In order to further modulate bandgap and promote surface photocatalysis of BiOBr, heteroatom doping [1, 10-17] or surface hybridisation with small-bandgap semiconductors or metal nanoparticles [18-21] were attempted successfully. Moreover, the heterogeneous photocatalysis usually involves multiple active species, including photogenerated charge carriers (e^{-1} and h^{+}) and derived active intermediates, though their respective roles in the photocatalysis are under debating [10, 22]. For instance of photocatalytic dye degradation, the photoexcited dye can transfer e^{-1} or h^{+} to CBM or VBM of semiconductor photocatalysts, though the dye-sensitisation effects were not paid enough attention when assess the performance of photocatalysts[8, 23]. Therefore, it is indispensible to unravel the relevance of photocatalysis with bandstructure and active intermediates to propose a reasonable photocatalysis mechanism[24, 25].

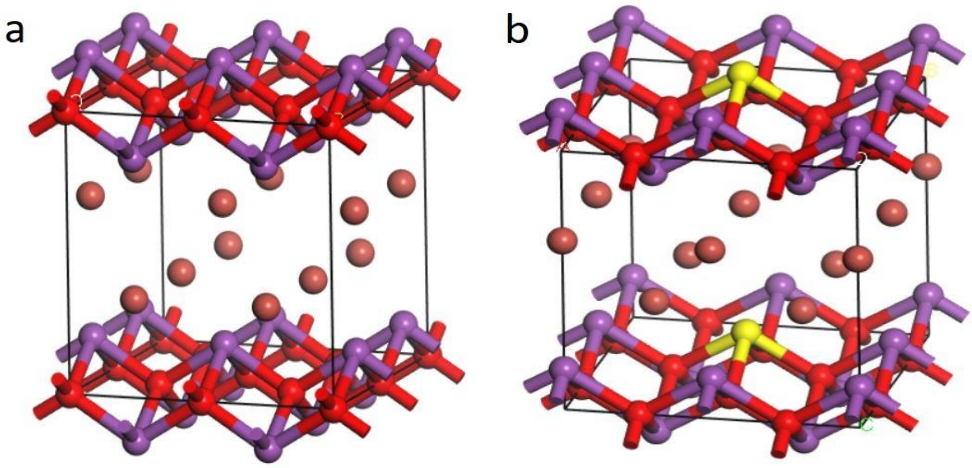

Figure 1 The ball-stick crystal models of BiOBr (2×2×1) supercell (a) and the derived 1/8Zn-doped BiOBr (b), where the purple, red, brown and yellow balls refer to Bi, O, Br and Zn atoms.

Comparing to surface metallisation and hybridisation, doping BiOBr with heteroatom are very convenient for practical applications [10, 19, 26, 27] because doping to BiOBr can occur even at ambient conditions. Compared to partial substitution of Br or O via mono- or co-doping of Cl, I, N or S[10, 14], the substitutions of Bi by metal are redeemed more flexible to tune the optoelectrical and catalytic properties of Bi-based oxyhalides (BiOX) [4, 10, 12, 13, 15, 28]. Previous DFT simulations suggested transition metal or rare earth dopants (eg, Ti, Fe, Mn, Eu, etc) with unclosed *d* and *f* valance electrons can introduce midgap energy levels to the bandstructure of pristine bismuth oxyhalides (BiOX, X=Cl, Br, I) [5, 6, 29, 30]. However, Zn possesses closed $3d^{10}$ and $4s^2$ electronic states that

are supposed to alter the bandstructure of BiOBr distinctive from other metallic dopants mentioned above, therefore, the particular attention was paid to Zn-doped BiOBr in this work.

Although enhanced visible-light photodegradation of RhB was observed on the flower-like Zn-doped BiOBr, which was attributed to their large surface areas and enhanced e^--h^+ separation[16], the results need further interpretation in terms of the charge carriers or active species. Controversially, Zn-doped BiOBr (Zn-BiOBr) displayed lower RhB photodegradation activity than BiOBr, which was attributed to H_2O_2 based reactive hydroxyl radical ($\cdot OH^-$)[31]. Using the widely adopted semi-empirical electronegativity methods [3, 10, 27, 32, 33], the latter research also illustrated the bandstructure of BiOBr and Zn-BiOBr with suitable CBMs and VBMs which show potentials enabling dye decomposition and water splitting. These controversial results further motivated us to examine Zn-doping effects on RhB photodegradation and water splitting.

Because the CBM and VBM are pivotal in interpret photocatalytic dye degradation and solar fuels [34], it is necessary to gain deep insights of Zn-doping effects on bandstructures of BiOBr and Zn-doped BiOBr through comparative simulations by state-of-the-art DFT program[4-6, 28, 30], to compare with the experimental bandstructures from spectral and photoelectromistry characterisations as well. With UV-Vis spectral techniques, both X-ray photoelectronic spectrum (XPS) and photoelectrochemical characterisations have been evidenced effective and reliable measures to analyse energy band positions (Mott-Schottky Impedance Spectra) and e^--h^+ separation efficiency (chronoamperometry)[8, 35]. Moreover, photocatalytic experiments using suitable radical scavengers allow to identify the rate-limit reactive species in photocatalysis [36].

In this work, Zn-doped BiOBr samples were prepared and applied in photodegradation of RhB and water splitting. The pristine BiOBr and Zn-doped BiOBr with 1/8 and 1/16 fractions of Bi atoms substituted by Zn were comparatively characterised and simulated by DFT to gain explicit insights into Zn-doping effects. Using radical scavengers, the research also distinguished the effects of bandgap, reactive radicals and dye sensitisation on photocatalytic RhB degradation and water splitting.

2. Computational and Experimental

2.1 Computational details

The electronic structures of typical BiOBr and xZn-BiOBr samples were simulated using DFT method implementing CASTEP 16.1 code[37]. The supercells of the primitive BiOBr cell were applied to build the Zn-doped BiOBr crystal models, where one Zn atom substitution of one Bi atom in the (2×2×1) and (2×2×2) supercells will create the respective original models of 1/8Zn-BiOBr (illustrated in Fig. 1 as an example) and 1/16Zn-BiOBr, corresponding to 1.04 and 2.08 atm% doping levels.

In the simulation, GGA-PBE exchange-correlation functional and norm-conserving pseudopotentials were used for geometry optimisation and electronic structure calculations, with considerations of electron spin polarization. For the geometry optimisation using BFGS method, the energy cut-off for the plane wave expansion was set to be 750 eV, resulting in a convergence of total energy and residual force tolerance to be within 0.1 eV/atom and 2.0×10^{-6} eV/angstrom, respectively. The *k*-point Monkhorst-Pack (MP) spacing of 0.125/Å was adopted when sampling in the Brillouin zones for geometry optimisation of the primitive BiOBr and the Zn-doped BiOBr supercells, while the *k*-point MP spacing of 0.0125/Å was adopted for band structure and density of states (DOS) calculations. The band structures were calculated along the Monkhorst-Pack (MP) grid connecting the high-symmetry k-points of Z (0,0,0.5), A (0.5,0.5,0.5), M (0.5,0.5,0), Γ (0,0,0), Z (0,0,0.5), R (0,0.5,0.5), X (0,0.5,0) and Γ (0,0,0) in the *k*-space of the first Brilluoin zone, where the two Γ points were applied because the MP grid should be closed.

2.2 Preparation of the Zn-doped BiOBr photocatalysts and photoelectrodes

The Zn-doped BiOBr photocatalysts with varying Zn-doping levels ($Zn_xBi_{(1-x)}OBr$, hereafter denoted as xZn-BiOBr, where x is the Zn-doping level) were prepared via a simple co-precipitation method. Typically, under rigorous stirring, 20 mL KBr (0.2 M)/NaOH (0.2 M) mixed solution was poured into 20 mL 20% acetic acid aqueous solution containing calculated amount of $Bi(NO_3)_3$ and $Zn(NO_3)_2$, where the Zn/Bi/Br molar ratios of x:(1-x):1 were maintained for obtaining xZn-BiOBr samples. Upon mixing the above solutions, pale yellowish precipitates were observed immediately, and the systems' final pH was adjusted to 12.0 using 0.3 M NaOH solution. The resulting mixtures were stirring for 6 h and ageing overnight before filtration and washing thoroughly by deionised water (DI). The received wet gels were dried in oven under 60 °C for 24 h to obtain the xZn-BiOBr photocatalysts.

The photoelectrodes of xZn-BiOBr photocatalysts were fabricated by doctor-blade coating of the photocatalyst pastes onto clean ITO/glass slices (1.5 cm x 1.5 cm, resistance of 15Ω/sq) which were pre-washed alternatively by absolute ethanol and DI water under ultrasonication (40 kHz, 5 min each). The pastes of photocatalysts were prepared by mixing 0.1 g photocatalysts with 100 μL ethanol/water (3:1) solution. 10 μL of photocatalyst paste was dropped on the dry clean ITO/glass fixed on flat bench using scotch tape to expose 1 x 1.5 cm^2 area, and then slowly rolled a clean glass rod to cast the film. The casted films were then dried at 60 ℃ for 24 h before photoelectrochemistry tests.

2.3 Characterisations

All the X-ray diffraction data were collected from the Rigaku SmartLab X-ray diffractometer, using Cu-Kα1 radiation (λ=0.154056 nm) and a scan rate of 0.05° 2θ/s, to determine the crystal phases of

the samples. The UV-vis diffuse reflectance spectra were obtained on Perkin Elmer Lambda 950 UV/Vis/NIR spectrophotometer equipped with a 150 mm snap-in integrating sphere for capturing diffuse and specular reflectance, where $BaSO_4$ was used as standard reflectance. The acquired lattice parameters and bandgap energies were listed in Table 1.

X-ray photoelectron spectroscopy (XPS) was performed on a Thermo Scientific Escaplab 250 K-alpha photoelectron spectrometer using monochromatic Al-Kα radiation. Survey and Valence band spectra were collected in the range 0–1100 eV (binding energy) at pass energy of 160 eV. Peak positions were calibrated to carbon and fitted using CasaXPS software. The morphologies of the samples were measured on JSM59 SEM manufactured by JEOL on which Energy Dispersive X-Ray (EDX) analyser was installed to analyse the composition of specimens in question.

2.4 Photocatalytic degradation of RhB and water splitting

The photodegradation of Rhodamine B (RhB) on the as-prepared samples was performed at ambient temperature under visible-light irradiation. A 300 W Xe lamp equipped with a 400 nm cut-off filter to remove UV light was used as light source, irradiating atop with light intensity of 30mW/cm^2 and 15 cm distance away from the beaker containing photocatalyst and RhB aqueous solution. In a typical photocatalysis experiment, 0.1 g of the photocatalyst powder was dispersed into 100 mL 20 ppm RhB aqueous solution. Before light irradiation, the mixed system was remained in dark for one hour to establish RhB adsorption-desorption equilibrium on catalyst surface. The initial concentration (C_0) was defined as the concentration of RhB upon adsorption-desorption equilibrium rather than the original concentration of RhB solution because the photocatalysis occurs on catalyst surface. In order to determine the temporal RhB concentration (C_t) at certain photo-reaction time (t) during photocatalysis, 4 mL liquid suspension was taken out every 3 mins and centrifuged under 6000 rmp to obtain supernatant solution for sampling by a UV-visible spectrophotometer (PerkinElmer Lampda 750s). Since photodegradation of dilute RhB in the aqueous solution is a pseudo-first-order reaction, the apparent kinetic coefficient (k) can be calculated form using the equation below:

$$-\ln\left(\frac{C_t}{C_0}\right) = \mathrm{kt} \qquad (1)$$

Radical scavenging experiments were conducted to identify the rate-limiting reactive species. Because ethylenediaminetetraacetic acid (EDTA), isopropanol (IPA) and p-benzoquinone (p-BQ) are effective scavengers with respective to h^+ at VBM, hydroxyl radical (•OH) and superoxygen radical due to e^- at CBM, they were mixed into RhB solution respectively to acquire corresponding photodegradation activities for comparing and assessing the contributions of photogenerated e^- [38] and h^+ [39] at band edges into photodegradation.

The experiments of photocatalytic hydrogen from water splitting were carried out in the similar procedure presented in the previous report [35]. Briefly, 100 mg of as-prepared photocatalysts was taken into a homemade reactor containing 80 mL deionized water and 20 mL methanol, to which $H_2PtCl_6 \cdot 6H_2O$ (0.5 wt% to photocatalysts) was added as a co-catalyst. Before photocatalytic testing, the reactor and the entire gas circulating system were de-aerated using a vacuum pump for 30 min. All photocatalytic H_2 generation tests were under continuous illumination using an Autolight CEL-HXF300 xenon lamp (300 W, 100 mW/cm^2) equipped with optical cut-off filters to realize visible light irradiation. The photocatalytic H_2 production was determined using Agilent gas chromatography (GC, 7900) at the sampling interval of 60 mins per test.

2.5 Photoelectrochemistry tests

Photoelectrochemistry measurements of the as-prepared BiOBr and Zn-doped BiOBr photoelectrodes were carried out at room temperature in a standard three-electrode cell using the AUTOLAB PGSTAT 302N equipped with FRA spectroscopy. The as-prepared film electrodes, a platinum disk and a saturated calomel electrode (SCE) were used as working electrodes, counter electrode and reference electrode, respectively. The electrolyte supporting solution was 100 mL 0.5 M Na_2SO_4 solution with constant pH of 6.5. The Mott-Schottky (M-S) data were acquired at the optimised frequency of 3000 Hz in dark, with 10 mV/s scan rate and 10 mV AC amplitude. The acquired potentials were transformed to reversible hydrogen electrode scale (RHE) to pH of 0.

The quantitative analysis of M-S data to acquire flat band potential (V_{fb}) is based on the Mott-Schottky law from the plots of C_{sc}^{-2} versus the applied potential bias (V_{app}):

$$\frac{1}{C_{sc}^2} = \frac{2}{A^2 \varepsilon_0 \varepsilon_r e N_d}\left(V_{app} - V_{fb} - \frac{k_B T}{e}\right) \quad (2)$$

where C_{sc}, A, N_d, ε_r and ε_0 are respective to the space capacitance, electrode area (1.0 cm^2 in this work), donor density, relative dielectric of semiconductor and vacuum dielectric, while the k_B, T and e stand for the Boltzmann constant (1.38x10^{-23} J/K), system absolute temperature (293 K here) and charge of electron (1.602x10^{-19} C). Extrapolation linear M-S plot to potential bias axis leads to an interception potential (V_{extro}, the corresponding charge energy of $E_{extro} = e \cdot V_{extro}$), while the slope of the M-S straight plot is proportional inversely to the density of majority carriers (N_d, e^- and h^+ for n-type and p-type semiconductor, respectively)[40]. The acquired E_{extro} can be manipulated by the following equations (the inferences were detailed in the ESI) to gain band edges in RHE scale.

$$E_{fb\sim SCE} = E_{extro} - k_B T/e \quad (3)$$

$$E_{fb\sim RHE} = E_{fb\sim SCE} + E^0_{SCE\sim RHE} + \frac{RT}{nF} pH \quad (4)$$

$$E_{CBM} = E_{fb\sim RHE} - 0.2eV \quad (5)$$

$$E_{VBM} = E_{CBM} + Eg \quad (6)$$

The equations 3~4 were applied to calibrate the potential contributions from temperature T (by $\frac{k_B T}{e}$ in eq. 3) and pH (by $\frac{RT}{nF} pH$ in eq.4), where R, n and F represent the universal gas constant, the number of electrons involved in the electrode reaction and the Faraday constant, respectively. In the equation (5), 0.2 eV was applied because the CBM potential is typical 0.2 V more negative than flat-band for most n-type semiconductors [40, 41]. The Eg, E_{CBM} and E_{VBM} are bandgap, energy positions of CBM and VBM, respectively. The retrieved data of BiOBr and the Zn-doped BiOBr were listed in Table 2.

The chronoamperometry tests (I-t plots) were recorded at light on-off cycle operation (on-off time interval of 20 s) at open circuit potentials (V_{OC}). The photocurrents acquired from Na_2SO_4 electrolyte solution containing RhB were applied to assess the dye-sensitisation effects. The corresponding chronoamperometrical results were summarised in Table 3.

3. Result and Discussion

3.1 Crystal structure and surface composition

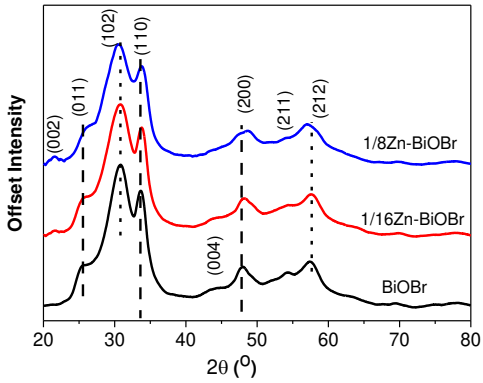

Figure 2 The XRD patterns of BiOBr and Zn-doped BiOBr samples

Fig. 2 presents the XRD data of the BiOBr and Zn-doped BiOBr samples, where all the characteristic diffraction peaks of the samples can be indexed to the tetragonal phase BiOBr (JCPDS 73-2061), without ZnO diffraction observed [11]. The gradual shifts of characteristic diffraction peaks and the interplane spacing distance shown in the HRTEM image of Zn-BiOBr (Fig. S1) suggest that Zn has been incorporated into the BiOBr matrix and caused distortion of BiOBr lattice [11]. The lattice parameters of BiOBr and Zn-doped BiOBr samples derived from XRD data are summarised in Table 1, further revealing that the Zn-doping induces shrinking of lattice parameters and distorts crystal structure. The unit cell shrinkages of the Zn-doped BiOBr samples can be well assigned to the substitutions of larger Bi^{3+} (1.03 Å) by smaller Zn^{2+} cation (radius of 0.74 Å)[42], which is in good agreement with DFT optimised geometric data and those of previous report [16].

Table 1 Experimental and computed lattice parameters and bandgap of pure and Zn-doped BiOBr

	a=b/Å	c/Å	c/a	V/Å^3	E_g/eV
BiOBr_Exp	3.7573	9.7672	2.5995	137.6224	2.42
	3.8377	9.4045	2.4506	138.5089	2.60
1/16 Zn-BiOBr	3.7421	9.2882	2.4821	130.0656	2.76
	3.8133	9.3998	2.4650	136.6849	2.67
1/8 Zn-BiOBr	3.7273	9.3503	2.5086	129.9015	2.87
	3.7945	9.3595	2.4666	134.7602	2.88

Note: the DFT simulated lattice parameters, cell volume and bandgap were listed in shadowed cells, while the experimental results were derived from XRD characterisations and Eg from UV-Vis spectra.

X-ray photoemission spectroscopy (XPS) was applied to analyse the surface elementary composition, the chemistry environment and the electronic interaction of BiOBr and Zn-doped BiOBr samples. The XPS survey spectra and core level XPS (Fig.S2 and S3) indicate that the samples with designed chemical composition were successfully prepared, in good agreement with the composition data acquired by EDS spectra as well (Fig. S4). Fig. 3(a~d) show the fitted core level XPS spectra corresponding to the Bi 4f, O 1s, Br 3d and Zn 2p core electron binding energies, which evidences cationic Zn was incorporated into BiOBr and systematically altered elemental binding energies (B.E.). The attributions of the core level XPS were presented in the electronic supporting information (ESI, S3). More importantly, significant and systematic red shifts of Bi, O, Br binding energies (Fig. 3a~c) are observed from the core-level XPS spectra of Zn-doped BiOBr, owing to the fact that Zn-dopant donates electrons to adjacent more electronegative Bi, O, Br atoms and thus enhances their core electron densities. The red-shifts of Br 3d binding energy may be partly arisen from the weakened Van de Walls forces between the $[Zn_{2x}Bi_{2-2x}O_2]^{(2-x)+}$ and Br^- slabs as Zn^{2+} substituting Bi^{3+}. The blue shifts of Zn 2p XPS (Fig. 3d) as increasing Zn-doping levels support the electron donation effects of Zn-dopant.

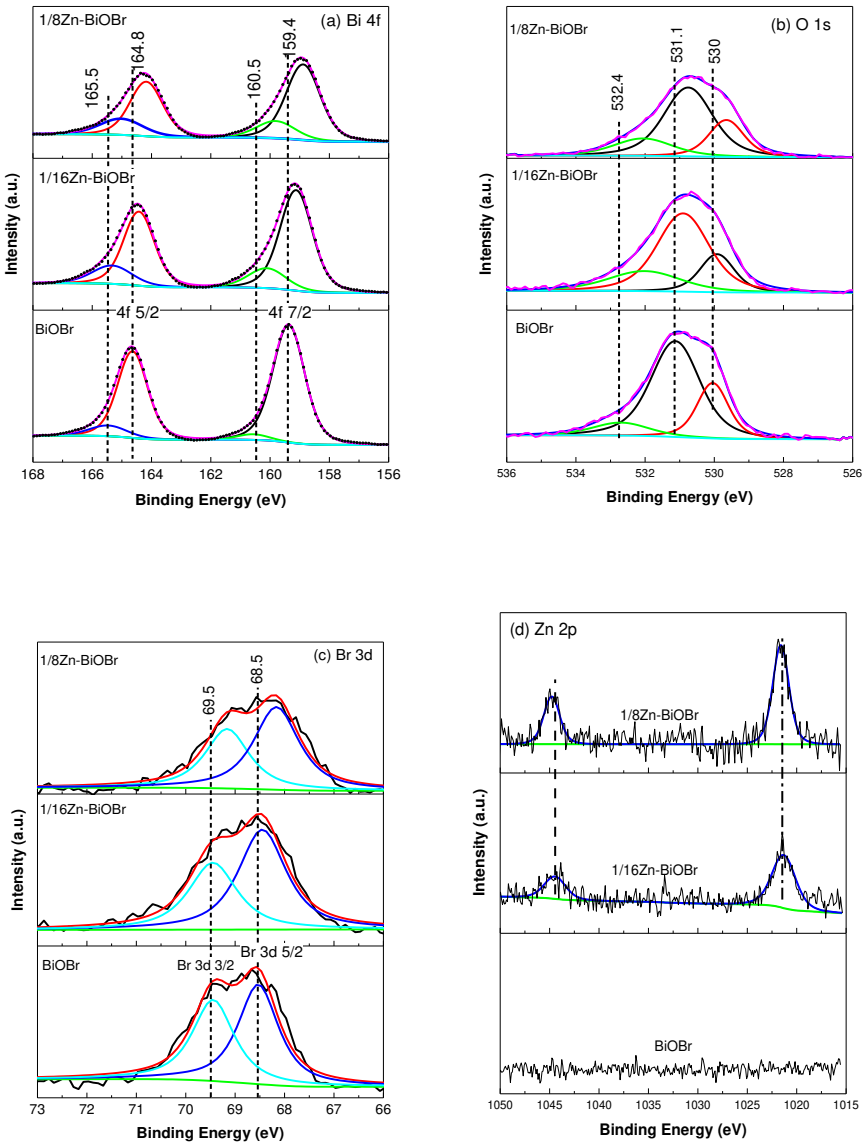

Figure 3 Core level XPS of Bi 4f (a), O1s (b), Br 3d(c), Zn 2p (d) of BiOBr and Zn-doped BiOBr samples

3.2 Optoelectronic properties

UV-Vis diffuse reflection absorbance spectra (UV-Vis-DRS) and corresponding Tauc plots were compared in Fig. 4 to gain light absorption properties and bandgap energies of the photocatalysts. In a broad wavelength region up to 600 nm, BiOBr exhibits stronger light absorption than Zn-doped BiOBr samples (Fig. 4a), suggesting that the increase of Zn-doping level causes gradual blue-shifts of the absorbance edges. However, the significant drifts in the absorbance spectra, which are due to the hue and specular reflection of the samples, hindered deriving accurate bandgap energies. The UV-Vis-DRS spectra were transformed into Tauc plots (Fig. 4b) implementing Kubelka-Munk equation. It was found Zn-doping did not change the indirect transition characteristic of BiOBr, as accordance with DFT calculations (see Fig. 5). The derived optical bandgap (Eg) of BiOBr is 2.42 eV, smaller

than those of the 1/16Zn-BiOBr (2.74 eV) and 1/8Zn-BiOBr (2.87 eV). The results suggest that Zn-doping broadens the bandgap of BiOBr, in coincidence with the Eg values reported for BiOBr and Zn-BiOBr samples via CTAB-directed synthesis[31]. However, the influences of Zn-doping on bandgaps of BiOBr in our work differ from those of the solvothermal-synthesised Zn-doped BiOBr nano-flowers[16]. Their smaller bandgaps of Zn-BiOBr nanoflowers are supposed to due to the hierarchical structure and the structure defects as reducing solvents involved therein.

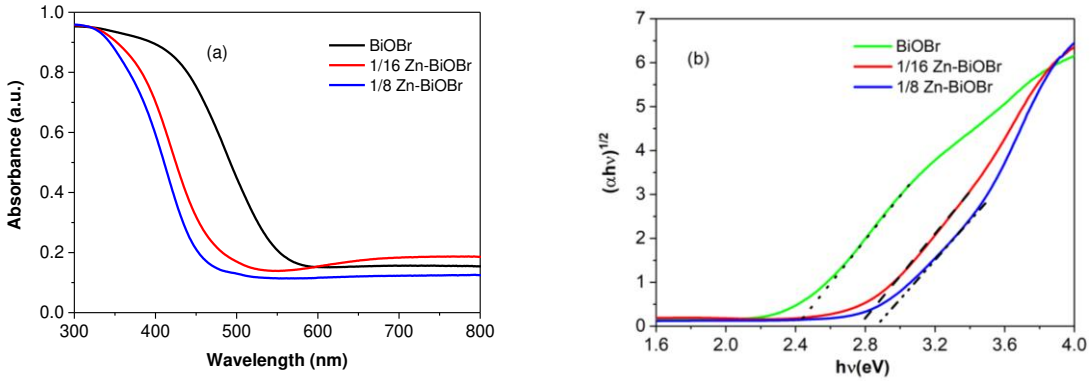

Figure 4 The UV-Vis absorbance (a) and tauc plots (b) of BiOBr and Zn-doped BiOBr samples.

Implementing GGA-PBE exchange-correlation functional in CASTEP16.1, the electronic structures of the materials simulated. As shown in Fig. 5, the computed electronic band-structures of BiOBr and Zn-doped BiOBr samples are projected in the first Brillion zone where Fermi energy levels were set at the top of VBM for convenience. The electronic states at VBM and CBM of Zn-doped BiOBr are less dispersive (smaller curvature) than those of BiOBr, suggesting their corresponding VBM h^+ and CBM e^- are heavier and less active because the charge effective and mobility are directly proportional to the band wave curvature. The computed Eg values of Zn-doped BiOBr are larger than that of BiOBr, highly consistent with the experimental data (Table 1) [5, 6], which concretely support the experimental findings that Zn-doping broadens bandgaps.

In contrast, previous DFT research suggests that metal-dopants with partially occupied *d* or *f* shells narrow bandgap of BiOBr by introducing impurity-induced mid-gaps [4, 28]. There is no impurity mid-gap observed in band gap regions of Zn-BiOBr materials, which is reasonable because the electrons on closed *3d* orbitals of Zn are not interactive enough to bring electronic states to bandgaps. Zn $3d^{10}$ electrons are found mainly contributing to deeper bands, localizing at ~7 eV more positive (deeper) than VBM (Fig. S5). The total electron density of states (DOS) and Zn partial DOS (PDOS), as shown in Fig. S6, further confirm the negligible contributions of Zn 3*d* orbitals to bandgaps.

Furthermore, the simulated CB and VB band edges suggest that Zn-doping alters the bandgap transition path of BiOBr (Fig. 5). Within the first Brillion zone, the conduction band minima (CBMs)

of the BiOBr and Zn-doped BiOBr samples all locate at Z points, whereas Zn-doping leads to valance band maxima (VBMs) gradually shift from R towards Z point and reduced indirect transition path. The calculated transition results well accord to UV-Vis features (Fig. 4b): increasing Zn-doping levels decreases tangents (slopes) of Tauc plots in bandgap zones.

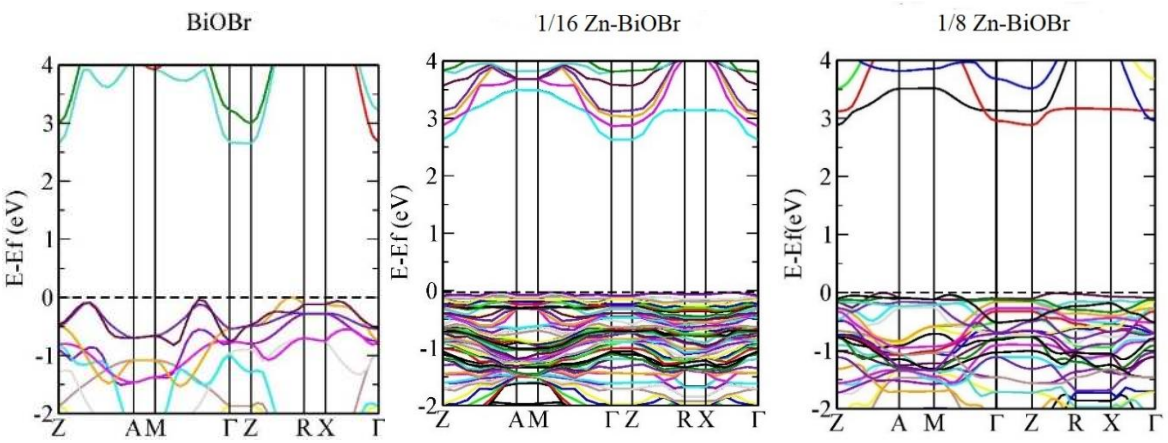

Figure 5 The DFT-simulated bandstructure of the BiOBr, 1/16Zn-BiOBr and 1/8Zn-BiOBr

As compared in Fig. 6, the total DOS and PDOS of pristine and Zn-doped BiOBr materials further reveal the effects of Zn-doping on the band structure. As shown in Fig. 6a, the CB and CBM of BiOBr are predominated by Bi 6*p* state, while VB and VBM are mainly occupied by Br 4*p* state with significant hybridisation with O 2*p* and Bi 6*s* electron states [5, 6]. In contrast, for the representative Zn-doped BiOBr (Fig. 6b), the Zn 4*s* electron states dominate CBM of Zn-doped BiOBr with stronger density and slightly hybridises with low-density Bi 6*p* state above CBM. In addition, the Zn-doping changes the electronic density and components of VB and VBM with slightly lower density of Br 4p, O 2p and Bi 6s states than those of BiOBr.

The Zn-dopant also broadens VB width, which was evidenced experimentally by the broader VB XPS of Zn-doped BiOBr (Fig. 6d). Comparing the XPS near VBM of the samples (Fig. 6d), one can conclude that Zn-doping pushes the VBM to deeper energy level (more positive), namely higher oxidation potential of VB holes. By extrapolating the valence band edge of the VBM XPS, the VBM potentials are determined of 2.05eV, 2.25eV and 2.31eV for BiOBr, 1/16Zn-BiOBr and 1/8Zn-BiOBr, respectively. Since XPS spectra were calibrated by C *1s* XPS (E_f of C is ~0.3 eV vs RHE), VBM potentials can then be transferred to 2.35, 2.55 and 2.61 eV in RHE scale, agreeing with Mott-Schottky measurements (Fig. 7). In addition, XPS at VBM edges of Zn-doped BiOBr samples show lower intensity than that of BiOBr, due to the reduced electronic density of Br 3*d*, O 2*p* and Bi 6*s* states which are caused by Zn-doping, as suggested by DOS results (Fig. 6 a~c).

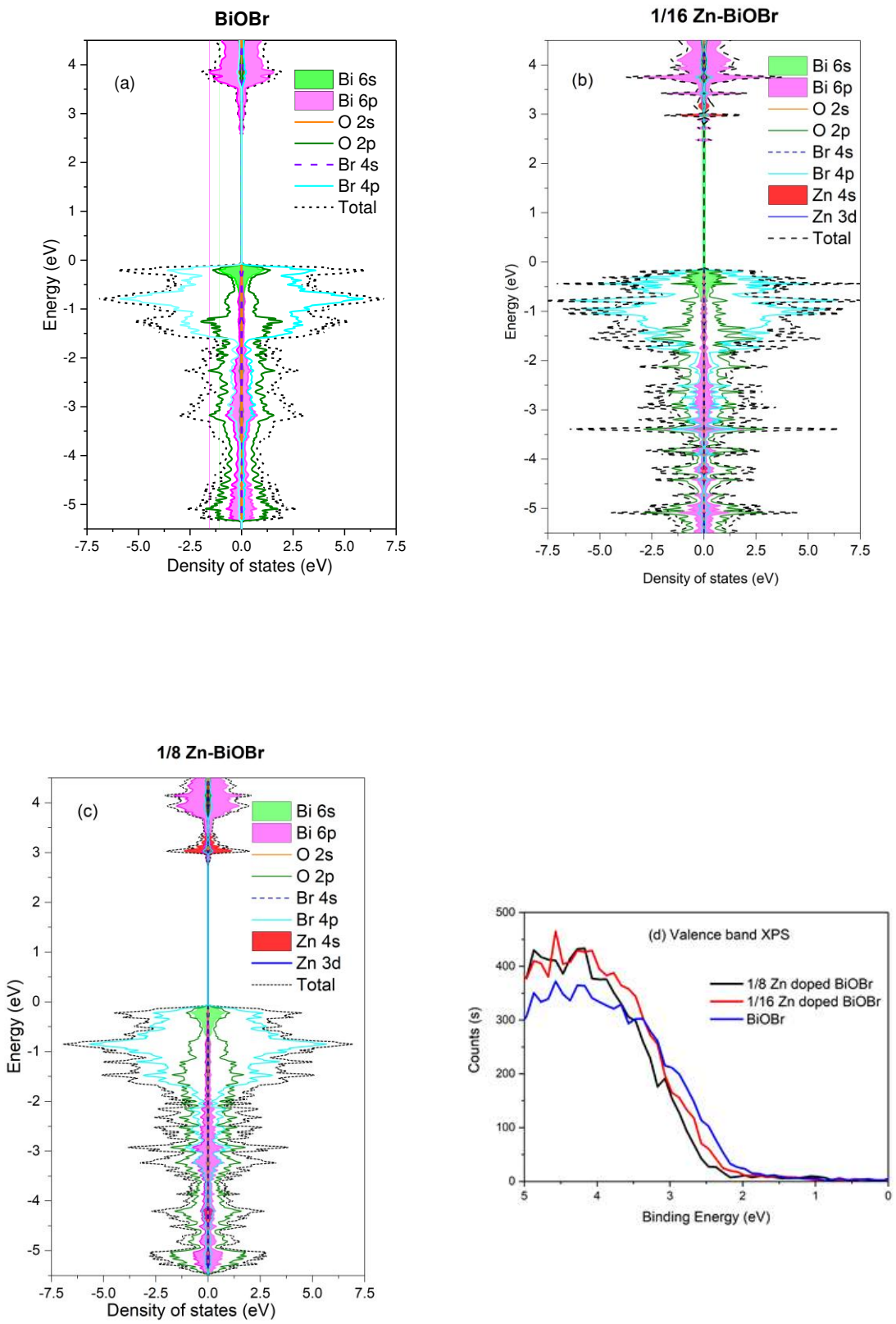

Figure 6 DOS and PDOS of BiOBr (a), 1/16Zn-BiOBr (b) and 1/8ZnBiOBr (c), where DOS of Bi and Zn are shadowed, and the VBM XPS of pristine and Zn-doped BiOBr samples (d).

Fig. 7a shows the Mott-Schottky (M-S) plots of BiOBr and Zn-doped BiOBr photoanodes, where the positive slopes of the linear regions reveal they are n-type semiconductors [43]. The tangent gradient becomes larger as increasing Zn-doping level in Zn-BiOBr samples, suggesting their electron donor density (N_d) from VB drops (Table 2) because of the tangent gradient is inversely proportional to majority density[44]. The results well agree with computed bandstructures and DOS of Zn-doped BiOBr where the flatter band edges suggest less dispersive and heavier h^+ occupied the VBMs [6].

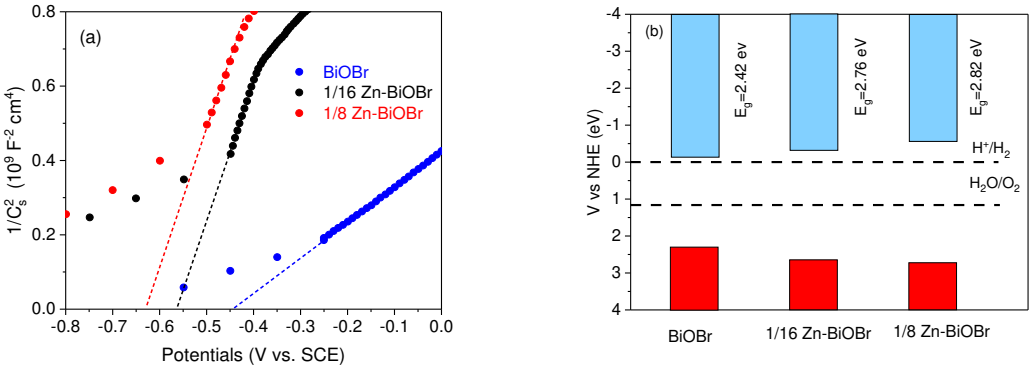

Figure 7 The photoanode Mott-Schottky plots (a) and the derived energy band diagrams vs RHE at pH=0 (b) of the BiOBr and Zn-doped BiOBr samples

The $E_{fb\sim RHE}$, E_{CBM} and E_{VBM} of the samples referring to RHE scale listed in Table 2 were extracted from the M-S plots. Accordingly, the energetic band diagram of BiOBr and Zn-doped BiOBr samples can be drawn and illustrated in Fig. 7b. Besides broadening the bandgap (Eg), increases of Zn-doping raise CBM of Zn-doped BiOBr to higher level (more negative) but push VBM energy downwards (more positive). The acquired VBM potentials are consistent with those from VB XPS, validating the M-S characterisation is an effective and reliable method to define the chemical potentials of VBM.

Table 2 Photodegradation rate constants and energy band edges (eV) of pure and Zn-doped BiOBr samples

Photocatalysts	**Rate constants (min^{-1})**	**$E_{extro\sim SCE}$**	**$E_{fb\sim RHE}$**	**$E_{CBM\sim RHE}$**	**$E_{VBM\sim RHE}$**	**M-S Slope**
BiOBr	0.1528	-0.45V	0.15	-0.05V	2.37 (2.35)	0.9570×10^9
1/16Zn-BiOBr	0.1357	-0.56V	0.04	-0.16V	2.60 (2.55)	3.7783×10^9
1/8Zn-BiOBr	0.1028	-0.62V	-0.02	-0.22V	2.65 (2.61)	3.2109×10^9

Note: The bracketed numbers in $E_{VBM\sim RHE}$ column were retrieved from VBM XPS spectra.

3.3 Photocatalytic water splitting and RhB decomposition

The band diagrams presented in Fig. 7b suggest the BiOBr and Zn-doped BiOBr can photocatalyticalyse water splitting [45]. Experimentally, higher photocatalytic hydrogen evolution rate was acquired (Fig. 8a) on the 1/16Zn-BiOBr (~29 μmol/g/h) with respect to BiOBr (~13 μmol/g/h). Considering the weaker PL intensity of 1/16Zn-BiOBr (Fig. S7) than that of BiOBr, the

enhanced water splitting on Zn-BiOBr can be assigned to the stronger redox ability of the photogenerated charge carriers (Fig. 7b) and the suppressed recombination of photogenerated charge carriers, which cancelled the influences from weaker light adsorption of Zn-BiOBr than BiOBr.

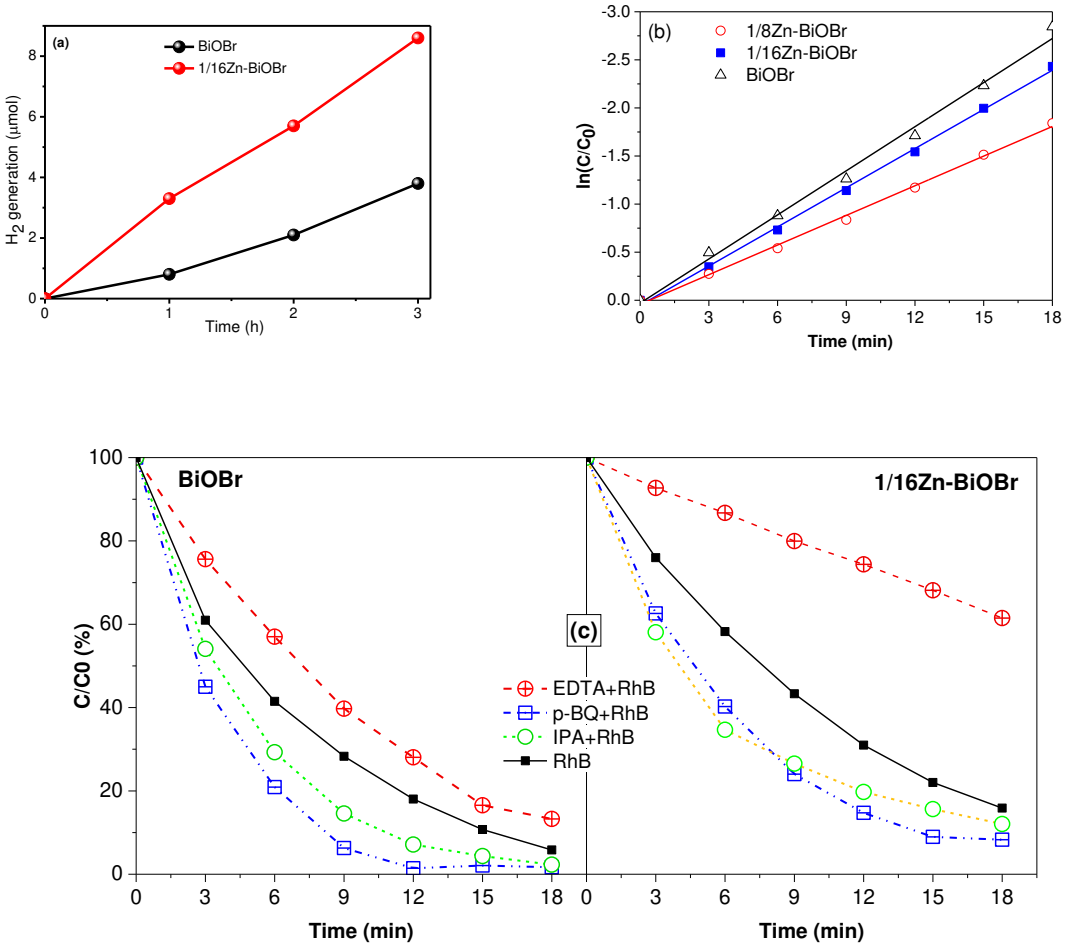

Figure 8 Visible-light photocatalytic water splitting (a) and RhB photodegradation on BiOBr and Zn-BiOBr samples: (b) apparent kinetic curves and (c) effects of adding radical scaverngers

Fig.8b comparatively shows the apparent photocatalysis kinetics of visible-light-driven photodegradation of RhB on BiOBr and the Zn-doped BiOBr samples. Since the samples displayed similar identical adsorption-desorption equilibrium (Fig. S8) and thus almost identical SSA, their apparent kinetic coefficients can be used to compare their intrinsic microscopic kinetic behaviour. The derived apparent kinetic coefficients (k, Table 2) suggest RhB photodegradation rate is dragged as Zn-doping levels increase, which agree with their apparent activity of RhB photodegradation (black lines in Fig. 8c and Fig. S9). Therefore, the stronger light adsorption of BiOBr seems responsible for its higher photocatalytic activity than Zn-doped samples, though such interpretation cannot clarify the mechanistic responsibility of the dye-sensitisation and photoexcitons for the redox half reactions.

4. Mechanism perspectives of photocatalysis in RhB photodegradation and H_2 evolution

It is a great challenge to unravel the photocatalytic mechanism in the aqueous photocatalytic system, because it contains aqueous radical intermediates, in particular the hydroxyl radical (HO•, 1.99 eV vs RHE), H_2O_2 (1.77 eV vs RHE) and superoxygen radicals ($\cdot O_2^-$, -0.046 eV vs RHE) [3]. The radicals possess strong redox power and can compete with e^- and h^+ from excited photocatalysts or dye. Comparing the redox potentials of the aqueous radicals with band edges of the photocatalysts (Fig. 7 b and Table 2), redox potentials of LUMO and HOMO of excited RhB and H^+, the major elementary reactions involved in the photocatalytic reactions are proposed and illustrated in Fig. 9.

4.1 Mechanism interpretation of H_2 evolution

From the chemical potential point of view, the bandstructure of BiOBr and Zn-BiOBr photocatalysts imply they can enable H_2 evolution from the methanol-sacrificial water splitting systems. On one hand, chemical potentials of photogenerated e^- from CBs of BiOBr and Zn-BiOBr photocatalysts are more negative than H^+ reduction ($E_{H^+/H2}$ = 0 eV *vs* RHE) (Fig. 9a), so H_2 was able to release in absence of other e^- scavengers (i.e. dissolved O_2) apart from H^+. On the other hand, methanol can largely scavenge h^+ accumulated on surface of the BiOBr-based photocatalysts, which facilitate e^- transferring to catalyst surface for proton reduction. Bearing in mind, the I-t plot (Fig. 10a) is not effective to interpret water splitting because methanol wasn't used in chronoamperometry tests.

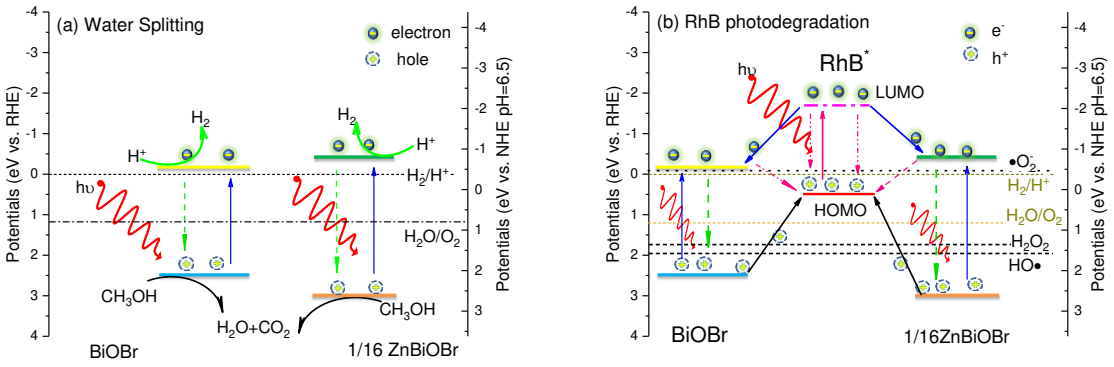

Fig. 9 The schematic mechanisms of photocatalytic water splitting (a) and RhB degradation (b)

The enhanced photocatalytic H_2 evolution due to Zn-doping can be interpreted from bandstructure and e^--h^+ recombination aspects. From the thermodynamic point of view, the H_2 evolution on Zn-BiOBr is more favourable, because the potential energy difference ($\Delta E_{CBM\sim H^+/H2} = E_{CBM} - E_{H^+/H2}$) between E_{CBM} and $E_{H^+/H2}$ on Zn-BiOBr is more negative than $\Delta E_{CBM\sim H^+/H2}$ on BiOBr, which is the driving force to promote photogeneration of H_2: First, photogenerated e^- from 1/16Zn-BiOBr is more reductive (E_{CBM} more negative, Fig. 9a) as compared to that of BiOBr. The more negative $\Delta E_{CBM\sim H^+/H2}$ on 1/16Zn-

BiOBr is helpful to limit the back reaction of H^+ reduction. Second and more importantly, the e^--h^+ recombination of BiOBr is nearly four-fold that of 1/16Zn-BiOBr as reflected by their PL spectra (Fig. S7). Such strong recombination on BiOBr would cancel its advantage on light absorption. Therefore, the higher reductive of CBM e^-, limited back reaction and larger amount of reactive e^- are responsible for superior H_2 evolution on Zn-doped to pristine BiOBr.

4.2 Mechanism interpretation of RhB photodegradation

For the energy downhill photodegradation of RhB, the competition of photoexcitons (e^--h^+) at band edges of photocatalysts with radical derivatives as well as dye photosensitisation effects can be defined from critical analyses of the results of radical scavenger and chronoamperometry experiments.

4.2.1 Rate-limiting species in RhB Photodegradation

As comparatively shown in Fig. 8c, photocatalytic activities on the pristine and Zn-doped BiOBr samples are found being enhanced significantly as adding either $\cdot O_2^-$ scavenger (p-BQ) or HO· (isopropanol, IPA) into respective RhB photodegradation systems [46]. These results can roughly rule out that $\cdot O_2^-$ and HO· radicals limit RhB photodegradation because the radicals were consumed rapidly by scavengers, leading to enhanced availability of photogenerated h^+. The p-BQ and IPA quenching experiments also reflect that photogenerated holes are perhaps rate-limiting species. The vital rate-determining roles of h^+ were verified by dramatically declined RhB degradation activity when adding EDTA-Na (h^+ scavenger) [16].

In the photocatalytic system, $\cdot O_2^-$ should be related to the photogenerated electrons at CBMs of BiOBr and Zn-BiOBr samples because their CBMs are more negative than $\cdot O_2^-$ formation energy (Fig. 9b). Taking account of the more negative LUMO of RhB (-1.77 eV vs RHE) than CBMs[47], the photogenerated electrons at CBM can be injected from both excited RhB (photosensitisation effects) and excited photocatalysts. The HOMO of RhB* (0.47 eV) is more positive than $\cdot O_2^-$ formation energy (-0.05 eV), so the recombination between the HOMO h^+ and $\cdot O_2^-$ can be occurred. However, the p-BQ can quench $\cdot O_2^-$ in the RhB photodegradation system that restrains the recombination as well as promote the VBM h^+, hence, p-BQ enhanced RhB photodegradation was observed.

The IPA enhanced RhB photodegradation likely follows the same mechanism if the photogenerated HO· radicals are induced by e^- from CBMs (Fig.9b). Since the HO· radical is more energetically positive than HOMO of RhB* but more negative than holes of photocatalysts VBMs, HO· radicals can accept holes from VBMs but cannot accept h^+ from HOMO of RhB*. However, the IPA quenched HO· radicals, which can consume more electrons and reduce their recombination to h^+ at VBMs as a result of IPA-enhanced RhB photodegradation on all the BiOBr-based samples (Fig. 8c).

The addition of EDTA caused more significantly decline of RhB photodegradation rate on the Zn-doped than the pristine BiOBr, indicating VBM holes are rate-limiting species for the present photodegradation reaction. This is reasonable because VBM of Zn-BiOBr is more positive and holes more oxidative than those of BiOBr and RhB HOMO (Fig.9b). Although the above apparent photocatalysis and scavenger experiments can roughly define the roles of reactive species, the RhB photosensitisation effects remains quantified insufficiently.

4.2.2 RhB dye photosensitisation effects

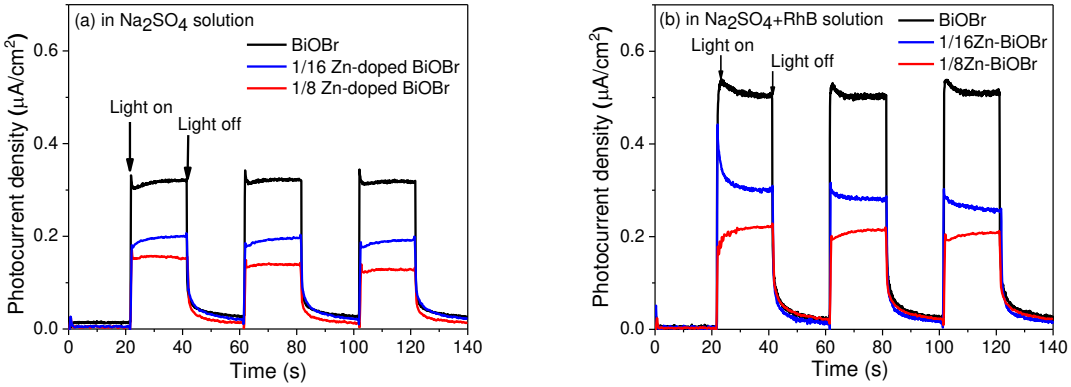

Figure 10 Temporary photocurrent density acquired on the BiOBr and Zn-doped BiOBr photoelectrodes in Na_2SO_4 electrolyte solutions without (a) and with 20 ppm RhB (b).

Table3 Temporal photocurrents on the pristine and Zn-doped BiOBr photoelectrodes

Photocatalysts	Photocurrent density (J, μA/cm^2) [a]			
	J_{PC}	$J_{RhB/PC}$	ΔJ[b]	$\Delta J/J_{PC}$ (%)[c]
BiOBr	0.32	0.51	0.19	+59.4%
1/16Zn-BiOBr	0.19	0.30	0.11	+57.9%
1/8Zn-BiOBr	0.13	0.21	0.08	+61.5%

Note: a.) The photocurrent density (J) data were collected at V_{OC} of corresponding photoelectrode, where J_{PC} and $J_{RhB/PC}$ represent J values acquired in 0.5 M Na_2SO_4 without and with 20 ppm RhB solution, respectively. b.) The absolute photocurrent density enhancement due to dye-sensitisation, $\Delta J = J_{RhB/PC} - J_{PC}$. c.) The relative enhancement in percentage due to dye-sensitisation, calculated by $\Delta J/J_{PC} * 100\%$.

The dye photosensitisation effects on the RhB photocatalytic degradation over the BiOBr-based photocatalysts were evaluated by chronoamperometrical experiments at open circuit potentials (V_{OC}). Fig. 10 shows the acquired temporary photocurrent density against light on-off time (J-t plots) of the BiOBr-based photoelectrodes in 0.5 M Na_2SO_4 without (Fig. 10a) and with (Fig. 10b) 20 ppm RhB

(denoted as J_{PC} and $J_{RhB/PC}$, respectively), which reflect the charges effectively separated and transferred onto the photocatalysts surface. Apparently, RhB photosensitisations dramatically promote the photocurrent density on all the BiOBr and Zn-doped BiOBr samples, in the 57%~62% enhancement range ($\Delta J/J_{PC}$ x100%). Although the relative enhancement ratios are comparable, the quantitative comparison of the photocurrents (Table 3) suggests the absolute photocurrent density enhancements (ΔJ) due to dye photosensitisation declines as increasing Zn-doping level.

5. Conclusion

The Zn-doping effects on RhB photodegradation over Zn-doped BiOBr, synthesised via a simple alkaline co-precipitation method, was convincingly clarified from energy and reactive species perspectives, through comprehensive spectral, DFT and photoelectrochemical investigations on the crystal structure, optoelectronic properties and photoelectrocatalysis of pristine and Zn-doped BiOBr. Under visible-light illumination, the Zn-doping in BiOBr was found showing higher H_2 evolution activity than BiOBr but detrimental activity in RhB photodegradation.

The comparative experimental and DFT characterisations of pure and Zn-doped BiOBr revealed that Zn-doping shrinks the lattice of BiOBr thought Zn-doped BiOBr samples remain indirect bandgap charge transitions. Distinct from the doping effects of other metals with unclosed d or f electronic shells, the Zn-doping in BiOBr was found expanding the bandgap by enhancing CBM and deepening VBM: The CBMs of Zn-doped BiOBr mainly compose of Zn 4*s* electron state with slight hybridisation to lower Bi 6*p* state that predominates the CBM of BiOBr, while VBMs of Zn-doped BiOBr comprise Br 3d, O 2p and Bi 6s states which is very similar to BiOBr except for reduced density due to Zn-doping. It was also found that the closed Zn $3d^{10}$ electrons locating in deeper band with negligible influence on VBM with respective to BiOBr while Zn-dopant donates core electrons to surrounding atoms.

The enhanced water splitting on Zn-doping to BiOBr in the methanol-sacrificial photocatalytic systems were attributed to the higher reactivity of charge carriers on band edges, the reduced back reaction of proton photo-reduction and the lower recombination of charge carriers on Zn-doped BiOBr, which altogether contributed more than light absorption in water splitting. However, the rate-limiting reactive species were confirmed photogenerated holes on the BiOBr-based materials in spite of multiple reactive radicals involved in the complex dye photodegradation system. The detrimental photocatalytic activities on Zn-doped BiOBr samples were reasonably attributed to the comprehensive results of the weaker light absorption and reduced dye-sensitisation effects besides the surface photogenerated electrons and holes.

Acknowledgements

This work was partially supported by the Zipler Institute grant at University of Southampton, the Newton Fund International Collaboration (NRCP1415/261) and the Royal Society International collaboration awards (IEC\NSFC\170670 and IE160277). JG and XL appreciate the Eustice studentship from Southampton University. The authors acknowledge the use of the IRIDIS High Performance Computing Facility and associated support services at the University of Southampton, in the completion of this work.

References

[1] D.S. Bhachu, S.J.A. Moniz, S. Sathasivam, D.O. Scanlon, A. Walsh, S.M. Bawaked, M. Mokhtar, A.Y. Obaid, I.P. Parkin, J. Tang, C.J. Carmalt, Bismuth oxyhalides: synthesis, structure and photoelectrochemical activity, Chem. Sci., (2016).
[2] J. Shang, W. Hao, X. Lv, T. Wang, X. Wang, Y. Du, S. Dou, T. Xie, D. Wang, J. Wang, Bismuth Oxybromide with Reasonable Photocatalytic Reduction Activity under Visible Light, ACS Catal., 4 (2014) 954-961.
[3] Z. Jiang, F. Yang, G. Yang, L. Kong, M.O. Jones, T. Xiao, P.P. Edwards, The hydrothermal synthesis of BiOBr flakes for visible-light-responsive photocatalytic degradation of methyl orange, J. Photoch. Photobio. A, 212 (2010) 8-13.
[4] Z.Y. Zhao, W.W. Dai, Structural, electronic, and optical properties of Eu-doped BiOX (X = F, Cl, Br, I): a DFT+U study, Inorg Chem, 53 (2014) 13001-13011.
[5] W.L. Huang, Electronic structures and optical properties of BiOX (X = F, Cl, Br, I) via DFT calculations, J. Comput. Chem., 30 (2009) 1882-1891.
[6] W.L. Huang, Q. Zhu, DFT calculations on the electronic structures of BiOX (X = F, Cl, Br, I) photocatalysts with and without semicore Bi 5d states, J Comput. Chem., 30 (2009) 183-190.
[7] J. Wang, N. Tafen de, J.P. Lewis, Z. Hong, A. Manivannan, M. Zhi, M. Li, N. Wu, Origin of photocatalytic activity of nitrogen-doped TiO2 nanobelts, J. Am. Chem. Soc, 131 (2009) 12290-12297.
[8] A.S. Alshammari, L. Chi, X. Chen, A. Bagabas, D. Kramer, A. Alromaeh, Z. Jiang, Visible-light photocatalysis on C-doped ZnO derived from polymer-assisted pyrolysis, RSC Adv., 5 (2015) 27690-27698.
[9] A. Dash, S. Sarkar, V.N. Adusumalli, V. Mahalingam, Microwave synthesis, photoluminescence, and photocatalytic activity of PVA-functionalized Eu3+-doped BiOX (X = Cl, Br, I) nanoflakes, Langmuir, 30 (2014) 1401-1409.
[10] C. Bi, J. Cao, H. Lin, Y. Wang, S. Chen, Tunable photocatalytic and photoelectric properties of I−-doped BiOBr photocatalyst: dramatic pH effect, RSC Adv., 6 (2016) 15525-15534.
[11] Z. Liu, B. Wu, Y. Zhao, J. Niu, Y. Zhu, Solvothermal synthesis and photocatalytic activity of Al-doped BiOBr microspheres, Ceram. Int, 40 (2014) 5597-5603.
[12] M.Q. He, W.B. Li, J.X. Xia, L. Xu, J. Di, H. Xu, S. Yin, H.M. Li, M.N. Li, The enhanced visible light photocatalytic activity of yttrium-doped BiOBr synthesized via a reactable ionic liquid, Appl Surf Sci, 331 (2015) 170-178.
[13] R.J. Wang, G.H. Jiang, X.H. Wang, R.B. Hu, X.G. Xi, S.Y. Bao, Y. Zhou, T. Tong, S. Wang, T. Wang, W.X. Chen, Efficient visible-light-induced photocatalytic activity over the novel Ti-doped BiOBr microspheres, Powder Technol, 228 (2012) 258-263.
[14] G.H. Jiang, X. Li, Z. Wei, X.H. Wang, T.T. Jiang, X.X. Du, W.X. Chen, Immobilization of N, S-codoped BiOBr on glass fibers for photocatalytic degradation of rhodamine B, Powder Technol, 261 (2014) 170-175.
[15] Z. Wei, G.H. Jiang, L. Shen, X. Li, X.H. Wang, W.X. Chen, Preparation of Mn-doped BiOBr microspheres for efficient visible-light-induced photocatalysis, MRS Commun., 3 (2013) 145-149.

[16] X.C. Song, Y.F. Zheng, H.Y. Yin, J.N. Liu, X.D. Ruan, The solvothermal synthesis and enhanced photocatalytic activity of Zn2+doped BiOBr hierarchical nanostructures, New J. Chem., 40 (2016) 130-135.
[17] G.H. Jiang, X.H. Wang, Z. Wei, X. Li, X.G. Xi, R.B. Hu, B.L. Tang, R.J. Wang, S. Wang, T. Wang, W.X. Chen, Photocatalytic properties of hierarchical structures based on Fe-doped BiOBr hollow microspheres, J. Mater. Chem. A, 1 (2013) 2406-2410.
[18] L. Ye, J. Liu, C. Gong, L. Tian, T. Peng, L. Zan, Two different roles of metallic Ag on Ag/AgX/BiOX (X = Cl, Br) visible light photocatalysts: Surface plasmon resonance and Z-Scheme bridge, ACS Catalysis, 2 (2012) 1677-1683.
[19] C. Yu, C. Fan, X. Meng, K. Yang, F. Cao, X. Li, A novel Ag/BiOBr nanoplate catalyst with high photocatalytic activity in the decomposition of dyes, Reaction Kinetics, Mechanisms and Catalysis, 103 (2011) 141-151.
[20] L. Lu, L. Kong, Z. Jiang, H.H.C. Lai, T. Xiao, P.P. Edwards, Visible-light-driven photodegradation of rhodamine B on Ag-modified BiOBr, Catal. Lett., 142 (2012) 771-778.
[21] L. Kong, Z. Jiang, H.H.C. Lai, T. Xiao, P.P. Edwards, Does noble metal modification improve the photocatalytic activity of BiOCl? Prog. Nat. Sci.: Mater. Intern., 23 (2013) 286-293.
[22] D. Jiang, L. Chen, J. Zhu, M. Chen, W. Shi, J. Xie, Novel p-n heterojunction photocatalyst constructed by porous graphite-like C3N4 and nanostructured BiOI: facile synthesis and enhanced photocatalytic activity, Dalton trans., 42 (2013) 15726-15734.
[23] S.K. Poznyak, A.I. Kulak, Photoelectrochemical properties of bismuth oxyhalide films, Electrochimica Acta, 35 (1990) 1941-1947.
[24] F.E. Osterloh, Photocatalysis versus Photosynthesis: A Sensitivity Analysis of Devices for Solar Energy Conversion and Chemical Transformations, ACS Energy Letters, 2 (2017) 445-453.
[25] K. Takanabe, Photocatalytic Water Splitting: Quantitative Approaches toward Photocatalyst by Design, ACS Catal., 7 (2017) 8006-8022.
[26] H. Cheng, B. Huang, Y. Dai, Engineering BiOX (X = Cl, Br, I) nanostructures for highly efficient photocatalytic applications, Nanoscale, 6 (2014) 2009-2026.
[27] L. Kong, Z. Jiang, H.H. Lai, R.J. Nicholls, T. Xiao, M.O. Jones, P.P. Edwards, Unusual reactivity of visible-light-responsive AgBr–BiOBr heterojunction photocatalysts, J. Catal., 293 (2012) 116-125.
[28] X.C. Zhang, C.M. Fan, Y.W. Wang, Y.F. Wang, Z.H. Liang, P.D. Han, DFT+U predictions: The effect of oxygen vacancy on the structural, electronic and photocatalytic properties of Mn-doped BiOCl, Comput. Mater. Sci, 71 (2013) 135-145.
[29] D.M. Jang, I.H. Kwak, E.L. Kwon, C.S. Jung, H.S. Im, K. Park, J. Park, Transition-Metal Doping of Oxide Nanocrystals for Enhanced Catalytic Oxygen Evolution, J. Phys. Chem. C, 119 (2015) 1921-1927.
[30] Z.Y. Zhao, Q.L. Liu, W.W. Dai, Structural, Electronic, and Optical Properties of BiOX1-xYx (X, Y = F, Cl, Br, and I) Solid Solutions from DFT Calculations, Sci. Rep., 6 (2016) 31449.
[31] W. Li, Y. Zou, X. Geng, F. Xiao, G. An, D. Wang, Constructing highly catalytic oxidation over BiOBr-based hierarchical microspheres: Importance of redox potential of doped cations, Mol. Catal., 438 (2017) 19-29.
[32] L. Kong, Z. Jiang, T. Xiao, L. Lu, M.O. Jones, P.P. Edwards, Exceptional visible-light-driven photocatalytic activity over BiOBr-ZnFe2O4 heterojunctions, Chem Commun, 47 (2011) 5512-5514.
[33] G. Jiang, R. Wang, X. Wang, X. Xi, R. Hu, Y. Zhou, S. Wang, T. Wang, W. Chen, Novel highly active visible-light-induced photocatalysts based on BiOBr with Ti doping and Ag decorating, ACS Appl. Mater. Interf., 4 (2012) 4440-4444.
[34] C. Piliego, M. Manca, R. Kroon, M. Yarema, K. Szendrei, M.R. Andersson, W. Heiss, M.A. Loi, Charge separation dynamics in a narrow band gap polymer-PbS nanocrystal blend for efficient hybrid solar cells, J. Mater. Chem., 22 (2012) 24411-24416.
[35] K.F. Zhang, W. Zhou, L.N. Chi, X.C. Zhang, W.Y. Hu, B.J. Jiang, K. Pan, G.H. Tian, Z. Jiang, Black N/H‐TiO2 Nanoplates with a Flower‐Like Hierarchical Architecture for Photocatalytic Hydrogen Evolution, ChemSusChem, 9 (2016) 2841-2848.

[36] T. Tan, D. Beydoun, R. Amal, Effects of organic hole scavengers on the photocatalytic reduction of selenium anions, J Photoch. Photobio. A, 159 (2003) 273-280.
[37] S.J. Clark, M.D. Segall, C.J. Pickard, P.J. Hasnip, M.I.J. Probert, K. Refson, M.C. Payne, First principles methods using CASTEP, Zeitschrift fur Kristallographie, 220 (2005) 567-570.
[38] Y. Kato, R. Nagao, T. Noguchi, Redox potential of the terminal quinone electron acceptor QB in photosystem II reveals the mechanism of electron transfer regulation, Proc Natl Acad Sci U S A, 113 (2016) 620-625.
[39] H.T. Hsu, S.S. Chen, Y.F. Tang, H.C. Hsi, Enhanced photocatalytic activity of chromium(VI) reduction and EDTA oxidization by photoelectrocatalysis combining cationic exchange membrane processes, J Hazard. Mater., 248-249 (2013) 97-106.
[40] J.H. Kennedy, Flatband Potentials and Donor Densities of Polycrystalline α-Fe[sub 2]O[sub 3] Determined from Mott-Schottky Plots, J. Electrochem. Soc., 125 (1978) 723.
[41] S.R. Morrison, Electrochemistry at semiconductor and oxidized metal electrodes, Plenum Press, 1980.
[42] R.D. Shannon, Revised Effective Ionic-Radii and Systematic Studies of Interatomic Distances in Halides and Chalcogenides, Acta Crystallogr. A, 32 (1976) 751-767.
[43] P. Kwolek, K. Szacilowski, Photoelectrochemistry of n-type bismuth oxyiodide, Electrochim. Acta, 104 (2013) 448-453.
[44] K. Gelderman, L. Lee, S.W. Donne, Flat-Band Potential of a Semiconductor: Using the Mott–Schottky Equation, J. Chem. Educ., 84 (2007) 685.
[45] X.Y. Kong, W.P.C. Lee, W.-J. Ong, S.-P. Chai, A.R. Mohamed, Oxygen-Deficient BiOBr as a Highly Stable Photocatalyst for Efficient CO2 Reduction into Renewable Carbon-Neutral Fuels, ChemCatChem, 8 (2016) 3074-3081.
[46] Q. Liu, Y.R. Guo, Z.H. Chen, Z.G. Zhang, X.M. Fang, Constructing a novel ternary Fe(III)/graphene/g-C3N4 composite photocatalyst with enhanced visible-light driven photocatalytic activity via interfacial charge transfer effect, Appl Catal B, 183 (2016) 231-241.
[47] H. Zhao, Y. Zhang, G. Li, F. Tian, H. Tang, R. Chen, Rhodamine B-sensitized BiOCl hierarchical nanostructure for methyl orange photodegradation, RSC Adv., 6 (2016) 7772-7779.